Rupture Process of the 2020 Caribbean Earthquake along the Oriente Transform Fault, Involving Supershear Rupture and Geometric Complexity of Fault

Tira Tadapansawut[1,1], Ryo Okuwaki[1,1], Yuji Yagi[1,1], and Shinji Yamashita[1,1]

[1]University of Tsukuba

November 30, 2022

Abstract

A large strike-slip earthquake occurred in the Caribbean Sea on 28 January 2020. We inverted teleseismic P-waveforms from the earthquake to construct a finite-fault model by a new method of inversion that simultaneously resolves the spatiotemporal evolution of fault geometry and slip. The model showed almost unilateral rupture propagation westward from the epicenter along a 300 km section of the Oriente transform fault with two episodes of rupture at speeds exceeding the local shear-wave velocity. Our modeling indicated that the 2020 Caribbean earthquake rupture encountered a bend in the fault system associated with a bathymetric feature near the source region. The geometric complexity of the fault system triggered multiple rupture episodes and a complex rupture evolution. Our analysis of the earthquake revealed complexity of rupture process and fault geometry previously unrecognized for an oceanic transform fault that was thought to be part of a simple linear transform fault system.

Rupture Process of the 2020 Caribbean Earthquake along the Oriente Transform Fault, Involving Supershear Rupture and Geometric Complexity of Fault

Tira Tadapansawut[1], Ryo Okuwaki[2,3,4], Yuji Yagi[2], and Shinji Yamashita[1]

[1]Graduate School of Life and Environmental Sciences, University of Tsukuba, Tsukuba, Ibaraki 305-8572, Japan.
[2]Faculty of Life and Environmental Sciences, University of Tsukuba, Tsukuba, Ibaraki 305-8572, Japan.
[3]Mountain Science Center, University of Tsukuba, Tsukuba, Ibaraki 305-8572, Japan.
[4]COMET, School of Earth and Environment, University of Leeds LS2 9JT, UK.

Corresponding author: Ryo Okuwaki (rokuwaki@geol.tsukuba.ac.jp)
Second corresponding author: Yuji Yagi (yagi-y@geol.tsukuba.ac.jp)

Key Points:

- We built a kinematic source model of the 2020 Caribbean earthquake to analyze the spatiotemporal evolution of fault geometry and slip
- A fault bend disturbed supershear rupture along the linear fault section and triggered subsequent rupture
- Oceanic transform faults can have geometric complexity that controls rupture evolution

Abstract

A large strike-slip earthquake occurred in the Caribbean Sea on 28 January 2020. We inverted teleseismic P-waveforms from the earthquake to construct a finite-fault model by a new method of inversion that simultaneously resolves the spatiotemporal evolution of fault geometry and slip. The model showed almost unilateral rupture propagation westward from the epicenter along a 300 km section of the Oriente transform fault with two episodes of rupture at speeds exceeding the local shear-wave velocity. Our modeling indicated that the 2020 Caribbean earthquake rupture encountered a bend in the fault system associated with a bathymetric feature near the source region. The geometric complexity of the fault system triggered multiple rupture episodes and a complex rupture evolution. Our analysis of the earthquake revealed complexity of rupture process and fault geometry previously unrecognized for an oceanic transform fault that was thought to be part of a simple linear transform fault system.

Plain Language Summary

On 28 January 2020, a large earthquake occurred on the Oriente fault, an oceanic transform fault in the Caribbean Sea between Jamaica and Cuba. The Oriente fault forms the boundary between the North America and Caribbean tectonic plates. The 2020 Caribbean earthquake was caused by horizontal sliding between the two plates. We used waveforms of the earthquake that were recorded around the world to build a model of the earthquake rupture process. The model showed that rupture during the earthquake was complex, featuring multiple rupture episodes with various rupture speeds and in various directions. Our model suggests that a bend in the fault was responsible for the changes of rupture speed and direction and the triggering of successive rupture episodes. Our analysis of the 2020 Caribbean earthquake has revealed complexity of both fault geometry and rupture process that were previously unknown in oceanic transform fault earthquakes.

1. Introduction

The Mid-Cayman Spreading Center is a passive rifted margin, where the oceanic lithosphere is juxtaposed against the continental lithosphere across the fracture zones with anomalously heterogeneous lithologic feature (Perfit and Heezen, 1978; Rosencrantz and Sclater, 1986; Rojas-Agramonte et al., 2005; Hayman et al., 2011; Grevemeyer et al., 2018; Peirce et al., 2019). The spreading develops a transform fault system (Peirce et al., 2019), and as a part of this system, Oriente transform fault sits in the northeast of Caribbean Sea (Fig. 1). The Oriente transform fault is characterized by anomalously flat and deep (> 6,000 m) bathymetric feature with a very high mantle Bouguer anomaly (Hayman et al., 2011; Peirce et al., 2019), and is also known to host moderate to large (moment magnitude $M_W \geq 6$) earthquakes as a result of left-lateral fault motion (Fig. 1). Thus, the Oriente transform fault zone provides an intriguing environment to study how these anomalous bathymetric feature and lithological heterogeneity relate to and/or control earthquake-rupture behaviors.

At 19:10:24 UTC on 28 January 2020, a large oceanic earthquake of a M_W 7.7 (USGS, 2020) occurred in the region of the Oriente transform fault. A moment tensor solution determined by the Global Centroid Moment Tensor (GCMT) project (Dziewonski et al., 1981; Ekström et al., 2012) indicates that the 2020 Caribbean earthquake was the result of strike-slip faulting on a vertical fault plane (GCMT, 2020; Fig. 1). A minor tsunami of 0.11 m height was recorded at tide gauges at Port Royal in Jamaica and at Puerto Plata in the Dominican Republic (NOAA, 2020). The aftershock distribution trended roughly west-south-west from the epicenter along the Oriente transform fault and some aftershocks were on the Cayman mid-ocean ridge (Fig. 1).

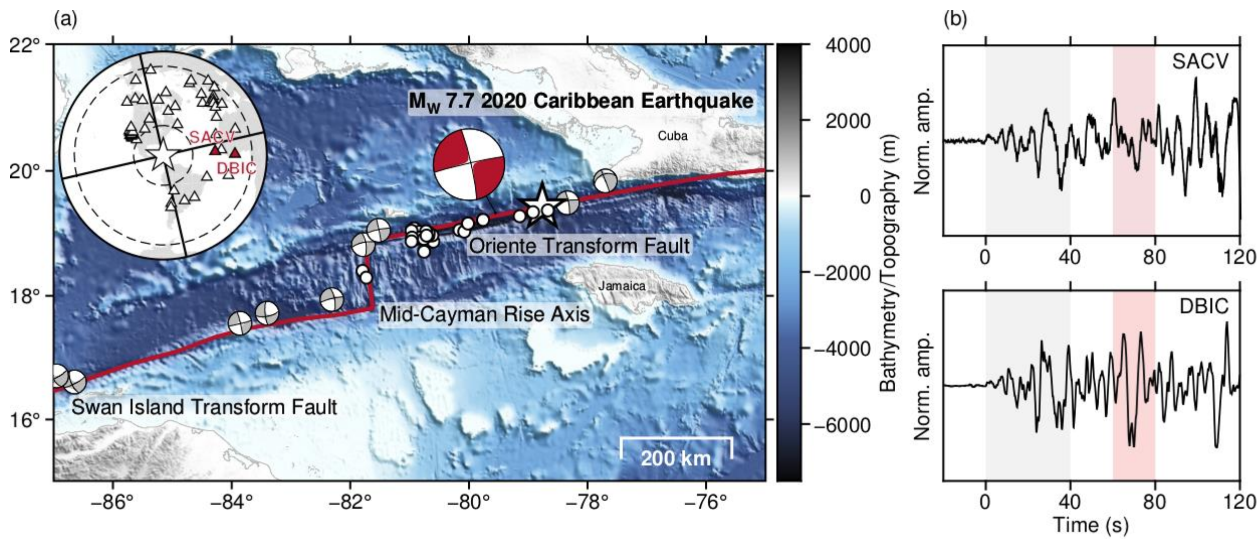

Figure 1. Overview map of the study area, station distribution, and selected waveforms. (a) Focal mechanisms (GCMT, 2020) of the mainshock (red) and previous major earthquakes (gray, $M_W \geq 6$) are presented as lower-hemisphere stereographic projections. The dots mark locations of the first week of aftershocks (USGS, 2020). Red lines are the transform faults and the ridge (Bird, 2003). Background topography/bathymetry is from GEBCO (2020). The inset shows the station distribution (triangle) and the epicenter (star) in azimuthal equidistant projection. The circles mark epicentral distances at 30° and 90°. Solid lines represent nodal directions at strikes of 77° and 167°. (b) Self-normalized waveform traces at the selected stations (red triangles in Fig. 1a). The gray and red shaded areas highlight the similarity and difference in waveform shape.

Oceanic transform faults have been fruitful environments for studies of earthquake-rupture dynamics because of their relatively linear fault geometry and structural heterogeneity (Abercrombie & Ekström, 2001; McGuire et al., 2012; Roland et al., 2012). Despite its apparent linearity of oceanic-transform-fault geometry, some cases of complexity in rupture dynamics have been identified. The M_W 7.1 2016 Romanche earthquake is a recent example of complex rupture on an oceanic transform fault, where a long initial rupture phase was followed by a back-propagating supershear rupture (Hicks et al., 2020). Another example is the M_W 7.7 2017 Komandorsky Islands earthquake, where the fault stepover in the transform fault system promoted a supershear transition (Kehoe & Kiser, 2020). Thus, the relationship between the geometric complexity of a fault system and its rupture process is worthy of investigation, even for oceanic transform fault earthquakes.

In Fig. 1b, we show teleseismic waveform data located at the similar azimuths and epicentral distances, which should be useful to simply evaluate the possible earthquake source characteristic without being contaminated by too many reflection/refraction phases, and with the well separated seismic phases to clearly show similarity and difference of waveform shape as indexes of source characteristics of the 2020 Caribbean earthquake. If we focus on the waveform feature during 0 to 40 s, the two share the similar shape, which is expected if these two stations are located in the same nodal sphere of the GCMT focal mechanism: strike/dip/rake 257°/87°/-5°. However in later larger phases, during 60 and 80 s, the waveform shape becomes different among the two stations, which is not expected if we only assume the one sole focal mechanism for the entire source process of the earthquake. This observation indicates that the focal mechanism of the 2020 Caribbean earthquake may have changed during the rupture evolution, which is possibly associated with the geometric complexity of the fault system. Thus, the 2020 Caribbean earthquake is a good candidate for investigation of possible complexity of the fault geometry of an oceanic transform fault earthquake and its role in rupture evolution.

In this study we inverted teleseismic waveform data from the 2020 Caribbean earthquake by applying a new method of finite-fault inversion (Shimizu et al., 2020) that represents fault deformation on an assumed fault by shear-slip vectors by superposition of five basis double-couple components. We showed that the geometric complexity of the Oriente transform fault controlled the multiple rupture episodes and supershear rupture that occurred during the earthquake. Our analysis of the 2020 Caribbean earthquake revealed previously unrecognized source complexity associated with complex fault geometry within an apparently simple oceanic transform fault system.

2. Data and Method

We downloaded vertical component of teleseismic waveform data from 52 stations of the Global Seismographic Network (GSN) and Federation of Digital Seismograph Network (FDSN) through the Incorporated Research Institutions of Seismology (IRIS) Data Management Center. Data were selected to ensure that azimuthal coverage (Fig. 1a) was sufficient to construct a finite-fault model.

To resolve possible changes of fault geometry during rupture propagation, we used the finite-fault inversion method of Shimizu et al. (2020), which can mitigate the effect of modeling errors associated with Green's function uncertainty (Yagi & Fukahata, 2011). This method can flexibly resolve fault geometry by representing the fault-normal and shear-slip vectors (potency density tensors defined by Ampuero & Dahlen, 2005) with five basis double-couple components of moment tensors (Kikuichi & Kanamori, 1991), rather than making an a priori assumption of fault geometry. In the prior constraints of Shimizu et al. (2020), a Gaussian with the same covariance was introduced into the instantaneous spatiotemporal variation of the slip-rate function without distinguishing between the five basis double-couple components. These constraints may, however, have introduced bias because the covariance that determines the smoothness variation for each basis slip component depends on the relative slip-rate of each component. In other words, the spatiotemporal slip-rate distributions of the dominant basis components become smoother than those of the minor basis components, which potentially biases the solution and makes it difficult to represent a complex rupture.

To mitigate this bias, we introduced new smoothness constraints by adding the relative standard deviation of each slip component proportional to each basis double-couple component of the GCMT solution for the 2020 Caribbean earthquake. To avoid instability of the solution due to an extremely small relative standard deviation, we set the relative standard variance of each basis component to be at least 10% of the maximum relative standard deviation. Because the GCMT solution shows dominantly strike-slip faulting, our new formulation takes the standard deviations of the two pure strike-slip components (M1 and M2 of Kikuchi and Kanamori, 1991) to be larger than those of the other slip components (Fig. S10); this enhances the contribution of strike-slip to resolve a possible change of fault geometry, which may have been masked by the artificially dominant dip-slip components in the original method. A comparison of the solutions obtained using our new smoothness constraints with those of the conventional constraints is presented in Figure S11.

We picked *P*-wave first arrivals manually and deconvolved the instrument response to velocity at a sampling interval of 1.0 s. Green's functions were calculated at a sampling interval of 0.1 s by the method of Kikuchi and Kanamori (1991). We use a finer sampling interval than that used for the observed waveforms, so that we ensure the sufficient resolution when convolving with basis slip-rate functions with the necessary time shift based on the relative sub-fault location to the hypocenter. After convolving with the basis slip-rate functions, the Green's functions in the kernel matrix are then resampled at 1.0 s, which is the same as the sampling rate of the observed data. We used the CRUST2.0 model (Bassin et al., 2000; USGS, 2020) as the one-dimensional layered medium near the source for calculating the Haskell propagation matrix for the Green's functions (Table S1). We do not apply any filters to both the observed waveforms and the theoretical Green's functions, following the processing in Shimizu et al. (2020), so that we retrieve the possible complexity of the source process recorded in the waveform data. A sensitivity of the one-dimensional layered medium near the source was tested by using the CRUST 1.0 model (Laske et al., 2013; Table S2). We found the model was insensitive to velocity structure (Fig. S9), which is consistent with the previous study, showing that teleseismic data is relatively robust against the assumption of structural velocity model, compared to the near-field records (Yagi et al., 2004). We assigned the model fault plane strike and dip angles of 77° and 90°, respectively. The length of the vertical model fault plane was 460 km along strike and it extended to 25 km depth. Sub-faults were 20 km along strike and 5 km along dip. The initial rupture point was placed at 15 km depth at 19.421°N and 78.763°W based on the epicenter determined by USGS (2020). We used a maximum rupture velocity of 6.0 km/s to allow for possible supershear rupture propagation. The slip-rate function for each sub-fault was a linear B-spline function of 61 s duration. Total rupture duration was 100 s. We evaluated the sensitivity of our model to different configurations of our model settings (see Figs. S2 to S9 and Text S1), as discussed in the following sections.

3. Results

Our source model for the 2020 Caribbean earthquake shows strike-slip faulting with almost unilateral westward propagation of rupture from the epicenter (Figs. 2 and 3). The total focal mechanism, which we calculated by integrating all of the potency density tensors (Fig. 2d), suggests strike-slip faulting with one of the nodal planes striking 258°. The total seismic moment was 0.124×10^{22} Nm (M_W 8.0), which is larger than the USGS W-phase moment tensor solution (USGS, 2020) and the GCMT solution (M_W 7.7). These differences of seismic moment can be explained by our selection of a wider model in both space and time to allow us to cover all possible rupture evolutions, for example, to allow for minor slip at the western extremity of the Oriente transform fault (Fig. 2a).

We grouped the rupture on the model fault plane into four zones along strike (Fig. 2d) on the basis of the spatial variation of nodal plane distribution extracted from the potency density tensor distribution: –300 to –220 km (zone A), –180 to –130 km (zone B), –120 to –20 km (zone C), and 60 to 100 km (zone D). The strike of maximum potency density changed successively from 78°, to 82°, to 84°, and to 100° from zone A to zone D (Fig. 2a). The changes along strike of the focal mechanism were well resolved, even when we changed the fault geometry and assumed velocity and duration of rupture (Figs. S2 to S9).

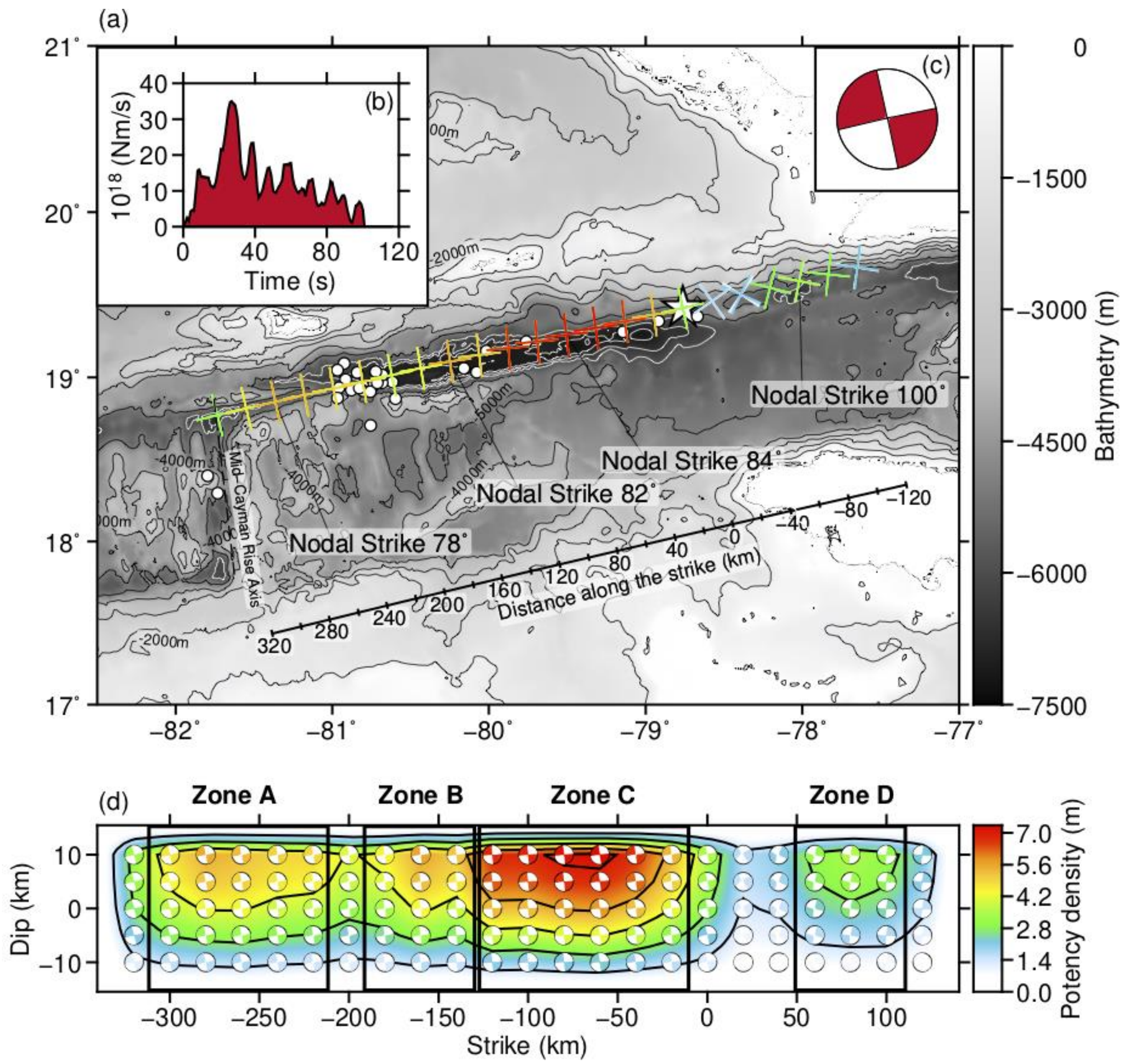

Figure 2. The static distribution of potency density. (a) The map view of static potency density distribution. The nodal planes (cross marker) for each location represent a potency density tensor.. The gray circle shows the 1-week aftershocks (USGS, 2020). The contour represents the bathymetry (GEBCO, 2020). White contours highlight iso-depths of 6000 to 7500 m every 500 m. (b) The moment-rate function. (c) The total moment tensor solution estimated from our finite-fault model, using a lower-hemisphere stereographic projection. (d) The cross-section of

the static potency density distribution. The focal mechanism is presented by the beach ball at each source knot, plotted using a lower-hemisphere stereographic projection, which are not rotated according to the model-plane geometry (not a view from side but from above). Panel height of Fig. 2d is magnified for the visibility of figure.

Snapshots of dynamic slip evolution (Fig. 3) show almost unilateral, westward rupture propagation. The initial rupture from 0 to 20 s propagated 80 km west from the epicenter with moderate potency-rate density and was followed by the main rupture episode from 20 to 30 s, about 100 km west of the epicenter, with maximum potency-rate density at 27 s, 80 km west of the epicenter. Fluctuations of potency-rate density between 40 and 80 s indicate several minor sources farther west from the epicenter, until the rupture ceased after 80 s about 300 km west of the epicenter.

The result showed the rupture-front speed was > 5 km/s for the initial rupture episode (0 to 20 s; Fig. 3b), which is faster than the local shear-wave velocity (~3 km/s at 15 km depth; Tables S1 and S2). Fast rupture propagation during the initial rupture episode was well reproduced for different assumed maximum rupture velocities (Fig. S2). Then, at the beginning of the main rupture episode (20 to 30 s), the westward propagating rupture front slowed down to 2.5 km/s between 20 and 25 s, and then accelerated again to > 5 km/s after 25 s.

The main rupture episode appears to have expanded both westward and eastward at about 40 s (Fig. 3b), which suggests bilateral rupture involving backward propagation, or a long-retained potency-rate density release of the initial rupture source (0 to 80 km west from the epicenter), or both. The spatiotemporal distribution of nodal planes extracted from the modeled potency-rate density tensors shows that their strike varied as the rupture front propagated along the Oriente transform fault (Fig. 3c). From 0 to 20 s, the nodal plane strike was 78°, from 20 to 30 s it rotated clockwise, reaching 83° about 100 km from the epicenter, where the highest potency-rate density was calculated. The strike then rotated counterclockwise to 79° from 45 to 50 s (240 km from the epicenter), which is similar to the strike we obtained near the epicenter (Fig. 3c). The rupture then continued to propagate westward until it reached the western end of the model fault plane.

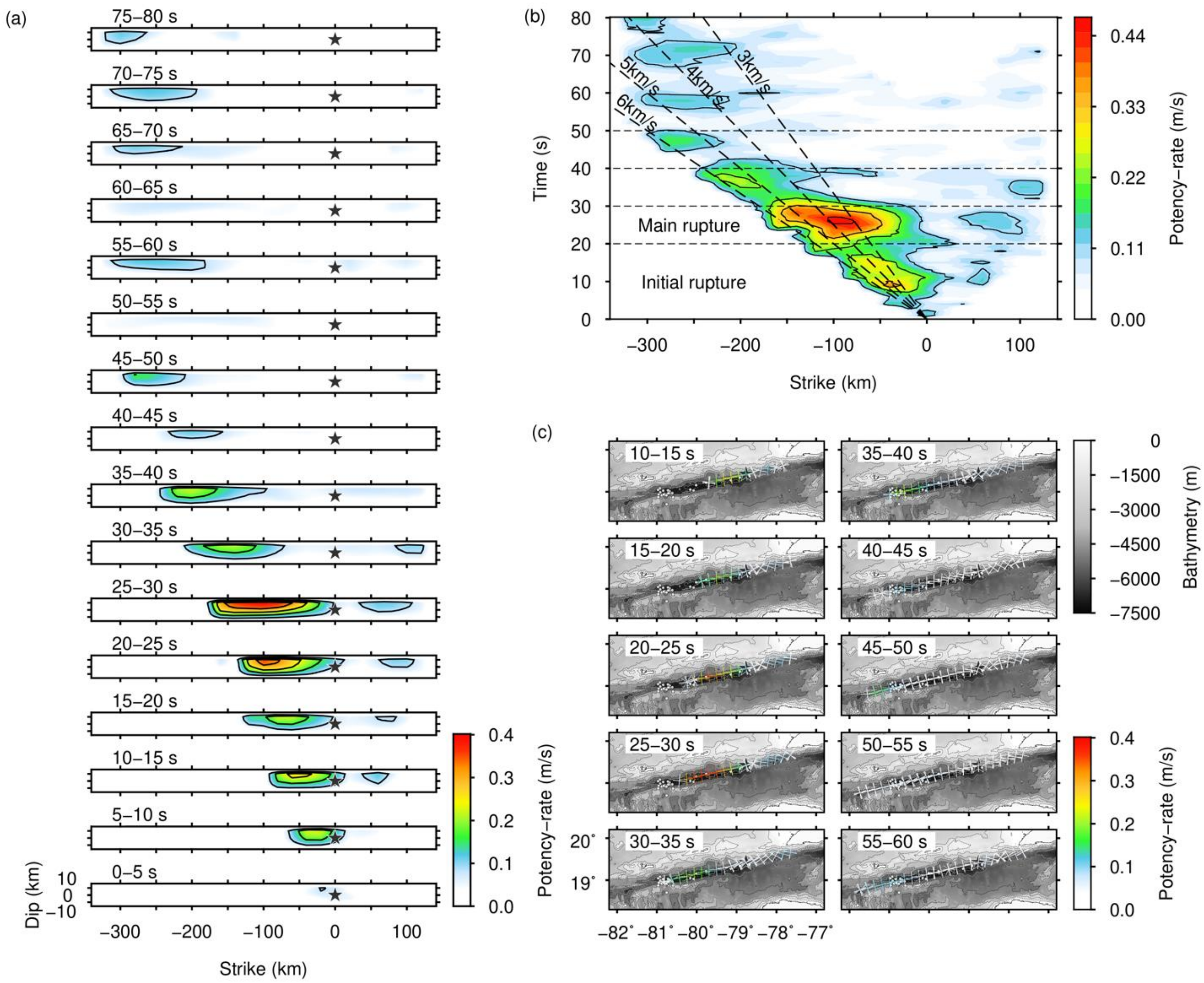

Figure 3. Spatiotemporal distribution of potency-rate density. (a) The snapshots of the rupture propagation. The potency-rate density is averaged within each time window. The star is the hypocenter, and the color contour shows the potency-rate density. (b) The potency-rate density distribution projected along the model strike. The black dashed lines represent the reference rupture speeds. (c) The map-view snapshots of the averaged potency-rate density within each time window. The cross marker shows the focal mechanism extracted from the resultant potency-rate density tensor. The background contour shows the bathymetry (GEBCO, 2020). The star and white dots denote the epicenter and the 1-week aftershocks (USGS).

4. Discussion

Our modeling of the spatiotemporal change of fault geometry during the 2020 Caribbean earthquake (Figs. 2 and 3) showed that the strike of the rupture surface deviated from the general strike of the Oriente fault system (~77°) in zone C (84°), 80 km west of the epicenter, and then returned to the general strike of the system in zone A, 280 km west of the epicenter (Fig. 2). These dynamic changes of fault geometry preceded periods of change of potency-rate density. For example, the change of strike that occurred from 20 to 25 s after the hypocentral time followed a period of relatively low potency-rate density (Fig. 3c), whereas the following change from 25 to 30 s was associated with the highest potency-rate density we obtained, which was between 60 and 160 km west of the epicenter. During the period from 40 to 50 s, the strike orientation returned to 78°, which is consistent with the general trend of the western end of the Oriente transform fault (~77°, in accord with the bathymetric feature 240 to 300 km west of the epicenter; Fig. 2a). After this transition of strike, we obtained a moderately high potency-rate density 280 km west of the epicenter. The transitions of fault geometry associated with lower potency-rate density correspond with the area of aftershocks of the 2020 Caribbean earthquake between about 140 and 200 km west of the epicenter (Fig. 2). Geometrical complexity in earthquake fault, including a fault bend, can affect the fluctuation of rupture propagation (Ulrich et al., 2019, Okuwaki et al., 2020). Simulations of dynamic fault rupture on strike-slip fault systems have demonstrated that an unfavorably oriented fault bend can reduce both the amount of displacement and the rupture speed (Bruhat et al., 2016; Duan & Oglesby, 2005; Kase & Day, 2006). The decrease of rupture speed between the initial and main ruptures (Fig. 3b) might be associated with geometric complexity in the Oriente fault system that prevented smooth rupture propagation and caused a stress change between the areas affected by the initial and main ruptures. The large deviation of the strike angles in zone D (Fig. 2) suggests that the causative fault geometry at the eastern edge of the source region should be discontinuous, which can work as a barrier to prohibit the further rupture evolution toward east from the epicentre, resulting in the asymmetric almost-unilateral rupture toward west.

The dominant potency-rate density release we modeled during the main rupture was within zone C, 25 to 30 s after the hypocentral time. The strike angle in zone C is 84°, which is 7° clockwise to the general strike angle of the Oriente fault (~77°), and then it returns to the general strike angle in zone A. The rupture of zone C continues with this strike angle over the length of about 120 km, which indicates that the distance to the Oriente fault axis is about 15 km at the west end of zone C. Given the relative fault motions around the west end of zone C, there should be subsidence around the west end of zone C, because the extensional (pull apart) motions inside the possible step of the fault could promote subsidence due to gravity. As shown in Fig. 2, the main-rupture region is located at the northern edge of the flat, deep trough region. The fault offset in zone C from the trough region would suggest that the 2020 Caribbean earthquake may have additionally induced subsidence at around the west end of zone C, and expanded the flat, deep trough. Although we do not have a direct evidence of the seafloor change after the 2020 Caribbean earthquake and it is not able to evaluate such a hypothesis at this moment, but our observation may provide an insight into the possible interaction between the earthquake rupture and the local bathymetric feature of the Oriente transform fault system. After the main rupture, the modeled potency-rate density decreased when it reached the position where the trough narrows abruptly (from 10 to 2 km wide) when it reached the eastern end of zone A. The western end of zone A is at the mid-Cayman rise axis, where crustal thickness decreases (ten Brink et al., 2002). The deviation of the fault geometry from the general trend of the Oriente transform fault is apparent in our modeling while the rupture follows the wider section of the trough, but to the west, as the rupture traverses the markedly narrower part of the trough and approaches the mid-Cayman rise, the amount of slip decreases and the fault geometry corresponds to the trend of the narrow trough. Thus, the rupture evolution of the 2020 Caribbean earthquake collectively suggests that fault geometry, even that of an oceanic transform fault, can change along strike in response to abrupt changes of the form of bathymetric features, which may be associated with fracture zones in the upper crust (Roland et al., 2012; van Avendonk et al., 2001).

Our modeling of rupture evolution showed rupture speeds faster than 5 km/s both from 0 to 20 s and from 25 to 40 s after initiation of rupture (Fig. 3b), which is faster than the local shear-wave velocity (~3 km/s at 15 km depth; Table S1). The fast velocity of rupture propagation was well resolved in our modeling, even with different assumed maximum rupture velocities (Fig. S2). Supershear rupture propagation has been identified in other strike-slip earthquakes (e.g., Bao et al., 2019; Bouchon et al., 2010; Kehoe & Kiser, 2020) and has been shown to activate aftershock clusters on secondary ruptures (Bouchon & Karabulut, 2008). Bouchon et al. (2010) reported that smooth fault geometry can promote supershear rupture; in particular, that linear fault geometry around an earthquake epicenter (as is the case for the general trend of the

Oriente transform fault) can lead to supershear rupture. Kehoe and Kiser (2020) suggested that a transition to supershear rupture in a fault system can also be associated with complex structural elements such as fault stepovers. Zones of damaged crust along a fault might also be responsible for supershear rupture (e.g., Huang et al., 2016); such zones can be features of a mature oceanic transform fault such as the Oriente transform fault (this study) and the Romanche transform fault (Hicks et al., 2020). However, the speed of westward propagation of the rupture front during the 2020 Caribbean earthquake decreased between 20 and 25 s after the hypocentral time (Fig. 3b) in an area where our modeling showed a change of fault geometry that may have temporarily restrained smooth rupture propagation, and then following supershear rupture proceeded toward farther west. The lithological heterogeneity of the transform fault system in the Mid-Cayman Spreading Center (e.g., Grevemeyer et al., 2018; Peirce et al., 2019) may also have largely controlled the complex rupture behavior, which is due to the contrast of material properties, as has been studied in the other transform fault earthquakes (Roland et al., 2012; McGuire et al., 2012; Hicks et al., 2020). Alternatively, it is possible that the main rupture of the 2020 Caribbean earthquake did not propagate as a continuation of the initial rupture; rather, it might have been dynamically or statically triggered by the initial rupture. Note that the main rupture is not only a pure unilateral but shows bilateral rupture toward both west and east (Fig. 3b). The eastern wing of rupture propagating back-toward the epicenter may have broken the region, in which the rupture was not able to propagate during the initial rupture episode, which may support the hypothesis that the main rupture is rather an individual rupture episode, involving a possible back-propagation of rupture (e.g., Hicks et al., 2020; Idini and Ampuero, 2020).

5. Conclusion

We used a newly developed method of finite-fault inversion to analyze the spatiotemporal evolution of fault geometry and slip during the 2020 Caribbean earthquake on the Oriente transform fault. We modeled successive changes of fault geometry during rupture and these changes controlled a rupture evolution that included a period of supershear rupture. Our study suggests that oceanic transform fault earthquakes, which have previously been thought to have relatively simple fault geometry and source processes, can have complex fault geometry and complex rupture processes associated with distinct bathymetric features.

Acknowledgments

We would like to thank the editor Germán Prieto, the associate editor, the reviewer Nick Hayman, and an anonymous reviewer for their constructive suggestions, which have led to significant improvements of the paper. This work has been supported by the Grant-in-Aid for Scientific Research (C) 19K04030. The facilities of IRIS Data Services, and specifically the IRIS Data Management Center, were used for access to waveforms, related metadata, and/or derived products used in this study. IRIS Data Services are funded through the Seismological Facilities for the Advancement of Geoscience (SAGE) Award of the National Science Foundation under Cooperative Support Agreement EAR-1851048. The figures were generated with the Generic Mapping Tools (Wessel et al., 2013).

Data Availability Statement

Teleseismic waveforms were obtained from the following networks : GEOSCPPE (G; https://doi.org/10.18715/GEOSCOPE.G); the Global Seismograph Network (GSN IRIS/IDA, II; https://doi.org/10.7914/SN/II); the Global Seismograph Network (GSN IRIS/USGS, IU; https://doi.org/10.7914/SN/IU); the Canadian National Seismograph Network (CN; https://doi.org/10.7914/SN/CN); the Czech Regional Seismic Network (CZ; https://doi.org/10.7914/SN/CZ); the Netherlands Seismic and Acoustic Network (NL; https://doi.org/10.21944/e970fd34-23b9-3411-b366-e4f72877d2c5); the Mediterranean Very Broadband Seismographic Network (MN; https://doi.org/10.13127/SD/fBBBtDtd6q); the Global Telemetered Seismograph Network (GTSN USAF/USGS, GT; https://doi.org/10.7914/SN/GT); the Southern California Seismic Network (CI; https://doi.org/10.7914/SN/CI); and the Berkeley Digital Seismograph Network (BK; https://doi.org/10.7932/BDSN). The moment tensor solutions are obtained from the GCMT catalog (https://www.globalcmt.org/CMTsearch.html). The Tsunami height is available by the NOAA (https://www.tsunami.gov). The CRSUT 1.0 and CRUST 2.0 structural velocity models are available through the websites (https://igppweb.ucsd.edu/~gabi/crust1.html) and (https://igppweb.ucsd.edu/~gabi/crust2.html), respectively.

References

Abercrombie, R. E., & Ekström, G. (2001), Earthquake slip on oceanic transform faults. *Nature*, *410*(March), 74–77, https://doi.org/10.1038/35065064.

Ampuero, J. P., & Dahlen, F. A. (2005), Ambiguity of the moment tensor. *Bulletin of the Seismological Society of America*, *95*(2), 390–400, https://doi.org/10.1785/0120040103.

Bao, H., Ampuero, J. P., Meng, L., Fielding, E. J., Liang, C., Milliner, C. W. D., Feng, T., Huang, H. (2019), Early and persistent supershear rupture of the 2018 magnitude 7.5 Palu earthquake. *Nature Geoscience*, *12*(March), 200–206, https://doi.org/10.1038/s41561-018-0297-z.

Bassin, C., Laske, G. and Masters, G. (2000), The Current Limits of Resolution for Surface Wave Tomography in North America, EOS Trans AGU, 81, F897. (No DOI is provided for this publication. Retrieved from https://igppweb.ucsd.edu/~gabi/crust2.html)

Bird, P. (2003), An updated digital model of plate boundaries, *Geochemistry Geophysics Geosystems*, 4(3), 1027, https://doi.org/10.1029/2001GC000252.

Bouchon, M., & Karabulut, H. (2008), The aftershock signature of supershear earthquakes. *Science*, *320*(5881), 1323–1325, https://doi.org/10.1126/science.1155030.

Bouchon, M., Karabulut, H., Bouin, M. P., Schmittbuhl, J., Vallée, M., Archuleta, R., Das, S., Renard, F., Marsan, D. (2010), Faulting characteristics of supershear earthquakes. *Tectonophysics*, *493*(3–4), 244–253, https://doi.org/10.1016/j.tecto.2010.06.011.

Bruhat, L., Fang, Z., & Dunham, E. M. (2016), Rupture complexity and the supershear transition on rough faults. *Journal of Geophysical Research*, *121*, 1–15, https://doi.org/10.1002/2015JB012512.

Duan, B., & Oglesby, D. D. (2005), Multicycle dynamics of nonplanar strike-slip faults. *Journal of Geophysical Research*, *110*(December 2004), 1–16, https://doi.org/10.1029/2004JB003298.

Dziewonski, A. M., Chou, T. A., & Woodhouse, J. H. (1981), Determination of earthquake source parameters from waveform data for studies of global and regional seismicity. *Journal of Geophysical Research*, *86*(B4), 2825–2852, https://doi.org/10.1029/JB086iB04p02825.

Ekström, G., Nettles, M., & Dziewoński, A. M. (2012), The global CMT project 2004-2010: Centroid-moment tensors for 13,017 earthquakes. *Physics of the Earth and Planetary*

Interiors, 200–201, 1–9, https://doi.org/10.1016/j.pepi.2012.04.002.

GCMT. (2020), Mw 7.7 Cuba Region. Retrieved January 28, 2020, from https://www.globalcmt.org/cgi-bin/globalcmt-cgi-bin/CMT5/form?itype=ymd&yr=2020&mo=1&day=28&oyr=1976&omo=1&oday=1&jyr=1976&jday=1&ojyr=1976&ojday=1&otype=nd&nday=1&lmw=7&umw=10&lms=0&ums=10&lmb=0&umb=10&llat=-90&ulat=90&llon=-180&ulon=180&lhd=0&uhd=1000&l.

GEBCO Compilation Group (2020), GEBCO 2020 Grid (Gridded Bathymetry Data Download), https://doi.org/10.5285/a29c5465-b138-234d-e053-6c86abc040b9.

Grevemeyer, I., Hayman, N. W., Peirce, C., Schwardt, M., Avendonk, H. J. A. Van, Dannowski, A., & Papenberg, C. (2018), Episodic magmatism and serpentinized mantle exhumation at an ultraslow-spreading centre. *Nature Geoscience*, *11*, 444–448. https://doi.org/10.1038/s41561-018-0124-6.

Hayman, N. W., Grindlay, N. R., Perfit, M. R., Mann, P., Leroy, S., & De Lépinay, B. M. (2011), Oceanic core complex development at the ultraslow spreading Mid-Cayman Spreading Center. *Geochemistry, Geophysics, Geosystems*, *12*(3), 1–21, https://doi.org/10.1029/2010GC003240.

Hicks, S. P., Okuwaki, R., Steinberg, A., Rychert, C., Abercrombie, R., Bogiaztis, P., Schlaphorst, D., Zahradnik, J., Kendall, J-M., Yagi, Y., Shimizu, K., Sudhaus, H. (2020), Back-propagating supershear rupture in the 2016 Mw 7.1 Romanche transform fault earthquake. *Nature Geoscience*, *13*(9), 647–653, https://doi.org/10.1038/s41561-020-0619-9.

Huang, Y., Ampuero, J.-P., & Helmberger, D. V. (2016). The potential for supershear earthquakes in damaged fault zones – theory and observations. *Earth Planet. Sci. Lett.*, *433*, 109–115. https://doi.org/10.1016/j.epsl.2015.10.046.

Idini, B., & Ampuero, J. P. (2020), Fault-zone damage promotes pulse-like rupture and back-propagating fronts via quasi-static effects. *Geophysical Research Letters*, https://doi.org/10.1029/2020GL090736.

Kase, Y., & Day, S. M. (2006), Spontaneous rupture processes on a bending fault. *Geophysical Research Letters*, *33*(10), 1–4, https://doi.org/10.1029/2006GL025870.

Kehoe, H. L., & Kiser, E. D. (2020), Evidence of a Supershear Transition Across a Fault Stepover. *Geophysical Research Letters*, https://doi.org/10.1029/2020GL087400.

Kikuchi, M., & Kanamori, H. (1991), Inversion of Complex Body Waves-III. *Bulletin of the Seismological Society of America*, *81*(6), 2335–2350. (No DOI is provided for this publication. Retrieved from https://pubs.geoscienceworld.org/bssa/article-lookup/81/6/2335)

Laske, G., Masters., G., Ma, Z. and Pasyanos, M. (2013), Update on CRUST1.0 -A 1-degree Global Model of Earth's Crust, Geophys. Res. Abstract, 15, Abstract EGU2013-2658. (No DOI is provided for this publication. Retrieved from https://igppweb.ucsd.edu/~gabi/crust1.html)

McGuire, J. J., Collins, J. A., Gouédard, P., Roland, E., Lizarralde, D., Boettcher, M. S., Behn, M. D., Hilst, R. D. Van Der. (2012), Variations in earthquake rupture properties along the Gofar transform fault, East Pacific Rise. *Nature Geoscience*, *5*(May), 336–341, https://doi.org/10.1038/ngeo1454.

NOAA. (2020), Mw7.7 U.S. Tsunami Warning System, Retrieved January 28, 2020, from https://www.tsunami.gov/events/PHEB/2020/01/28/20028001/5/WECA41/WECA41.txt.

Okuwaki, R., Hirano, S., Yagi, Y., & Shimizu, K. (2020), Inchworm-like source evolution through a geometrically complex fault fueled persistent supershear rupture during the 2018 Palu Indonesia earthquake. *Earth and Planetary Science Letters*, *547*, 116449, https://doi.org/10.1016/j.epsl.2020.116449.

Peirce, C., Robinson, A. H., Campbell, A. M., Funnell, M. J., Grevemeyer, I., Hayman, N. W., Van Avendonk H.J.A., Castiello, G. (2019), Seismic investigation of an active ocean-continent transform margin: The interaction between the Swan Islands Fault Zone and the ultraslow-spreading Mid-Cayman Spreading Centre. *Geophysical Journal International*, 219(1), 159–184. https://doi.org/10.1093/gji/ggz283.

Perfit, M. R., & Heezen, B. C. (1978), The geology and evolution of the Cayman Trench. *Geological Society of America Bulletin*, *89*, 1155–1174, https://doi.org/10.1130/0016-7606(1978)89<1155:TGAEOT>2.0.CO;2.

Rojas-Agramonte, Y., Neubauer, F., Handler, R., Garcia-Delgado, D. E., Friedl, G., & Delgado-Damas, R. (2005), Variation of palaeostress patterns along the Oriente transform wrench corridor, Cuba: Significance for Neogene-Quaternary tectonics of the Caribbean realm. *Tectonophysics*, *396*, 161–180, https://doi.org/10.1016/j.tecto.2004.11.006.

Roland, E., Lizarralde, D., Mcguire, J. J., & Collins, J. A. (2012), Seismic velocity constraints on the material properties that control earthquake behavior at the Quebrada-Discovery-Gofar transform faults, East Pacific Rise. *Journal of Geophysical Research*, *117*, 1–27, https://doi.org/10.1029/2012JB009422.

Rosencrantz, E., & Sclater, J. G. (1986), Depth and age in the Cayman Trough. *Earth and Planetary Science Letters*, *79*(1–2), 133–144, https://doi.org/10.1016/0012-821X(86)90046-4.

Shimizu, K., Yagi, Y., Okuwaki, R., & Fukahata, Y. (2020), Development of an inversion method to extract information on fault geometry from teleseismic data. *Geophysical Journal International*, *220*(2), 1055–1065, https://doi.org/10.1093/gji/ggz496.

ten Brink, U., Coleman, D. F., & Dillon, W. P. (2002), The nature of the crust under Cayman Trough from gravity. *Marine and Petroleum Geology*, *19*, 971–987, https://doi.org/10.1016/S0264-8172(02)00132-0.

Ulrich, T., Vater, S., Madden, E. H., Behrens, J., van Dinther, Y., van Zelst, I., Fielding, E. J., Liang, C., Gabriel, A. A. (2019), Coupled, Physics-Based Modeling Reveals Earthquake Displacements are Critical to the 2018 Palu, Sulawesi Tsunami. *Pure and Applied Geophysics*, *176*(10), 4069–4109, https://doi.org/10.1007/s00024-019-02290-5.

USGS. (2020), M 7.7 - 123km NNW of Lucea, Jamaica. Retrieved January 28, 2020, from https://earthquake.usgs.gov/earthquakes/eventpage/us60007idc/executive.

van Avendonk, H. J. A., Harding, A. J., Orcutt, J. A., & McClain, J. S. (2001), Contrast in crustal structure across the Clipperton transform fault from travel time tomography. *Journal of Geophysical Research: Solid Earth*, *106*(B6), 10961–10981, https://doi.org/10.1029/2000jb900459.

Wessel, P., W.H.F. Smith, R. Scharroo, J. Luis, and F. Wobbe. (2013), Generic Mapping Tools: *Improved Version Release, EOS Trans. AGU*, *94*(45), p.409-410, https://doi.org/10.1002/2013EO450001.

Yagi, Y., & Fukahata, Y. (2011), Introduction of uncertainty of Green's function into waveform inversion for seismic source processes. *Geophysical Journal International*, *186*(2), 711–720, https://doi.org/10.1111/j.1365-246X.2011.05043.x.

Yagi, Y., Mikumo, T., Pacheco, J., & Reyes, G. (2004), Source Rupture Process of the Tecomán, Colima, Mexico Earthquake of 22 January 2003, Determined by Joint Inversion of Teleseismic Body-Wave and Near-Source Data. *Bulletin of the Seismological Society of America*, 94 (5), 1795–1807, https://doi.org/10.1785/012003095.

Geophysical Research Letters

Supporting Information for

Rupture Process of the 2020 Caribbean Earthquake along the Oriente Transform Fault, Involving Supershear Rupture and Geometric Complexity of Fault

Tira Tadapansawut[1], Ryo Okuwaki[2,3], Yuji Yagi[2], and Shinji Yamashita[1]

[1]Graduate School of Life and Environmental Sciences, University of Tsukuba, Tsukuba, Ibaraki 305-8572, Japan.
[2]Mountain Science Center, Faculty of Life and Environmental Sciences, University of Tsukuba, Tsukuba, Ibaraki 305-8572, Japan.
[3]COMET, School of Earth and Environmental, University of Leeds LS2 9JT, UK.

Corresponding author: Ryo Okuwaki (rokuwaki@geol.tsukuba.ac.jp)
Second corresponding author: Yuji Yagi (yagi-y@geol.tsukuba.ac.jp)

Contents of this file

Introduction

Figure S1 shows the waveform fitting for the optimal finite-fault. The uncertainty analyses of the finite-fault inversion are summarized in Text S1, Figures S2 to S9, and Tables S1 to S2. Figure S10 visualizes the relative weights for the basis double-couple components adopted our new finite-fault inversion. Figure S11 shows comparison between the conventional and new results adopting the relative weights for the basis double-couple components.

Text S1. Uncertainty and sensitivity analyses of the finite-fault inversion

We tested assumption of maximum rupture velocity at 3, 4, 5, and 6 km/s (Fig. S2). The initial and main rupture episodes were robustly resolved for all the assumptions of maximum rupture velocity. The assumption of maximum rupture velocity did not affect the temporal location of the main rupture episode at ~20–30 s. For the slower rupture velocity (≤ 3 km/s), the spatial location of the main rupture was arbitrary confined by the assumption of maximum rupture velocity, but it stayed stable at -100 km to -50 km for the faster rupture velocity ≥ 4 km/s. Later stages of rupture (e.g., > 50 s) shows less stable than the initial and main rupture stages against the assumption of maximum rupture velocity. The slight difference of the model-fault geometry did not affect the solutions. We applied the alternative model-faults: strike/dip at 77°/87° and 257°/87° to test the sensitivity of the different dip angle assumption of the model fault planes (Fig. S3). The resultant of total focal mechanism, moment-rate function, large potency density zone and the strike orientation change were consistent to our assigned model-plane in this study (strike/dip = 77°/90°, Fig 2). We further tested the assumption of model-fault geometry by adopting the horizontal model fault dipping at 0° placed at 15-km depth, in order to evaluate the spatial extents of rupture. As shown in Figs. S4 and S5, the spatiotemporal location of the initial and main rupture episodes share the similar feature between the two; the one with 0°-dipping and the other with the vertical dipping. The strike orientation at -320 to -220 km westward of the epicenter is also consistent between the two. The consistency against the model faults adopting the different dip angles can be explained by the very narrow, confined width of the rupture area for the 2020 Caribbean earthquake, which shows the less variable rupture manner along the dip extent of the fault. Moreover, we have extended the length along the strike of the model fault plane covering the mid-Cayman rise axis to evaluate the rupture termination (Figs. S6 and S7). Even if we extended the western side of model-fault length, we did not resolve the significant potency density across the mid-Cayman rise axis after 50 s.

We tested the assumption of maximum duration of potency-rate density function at each subfault, by reducing from 61 s to 41 s (Fig. S8). We found the initial and main rupture episodes were robustly resolved in both space and time and not contaminated by the assumption of rupture duration.

The different near-filed structural velocity models of CRUST1.0 and CRUST2.0 (Tables S1 and S2) were also tested to evaluate the sensitivity (Fig. S9). Although we recognize the slight difference between them, but the assumption of near-field velocity structure did not significantly affect the solution.

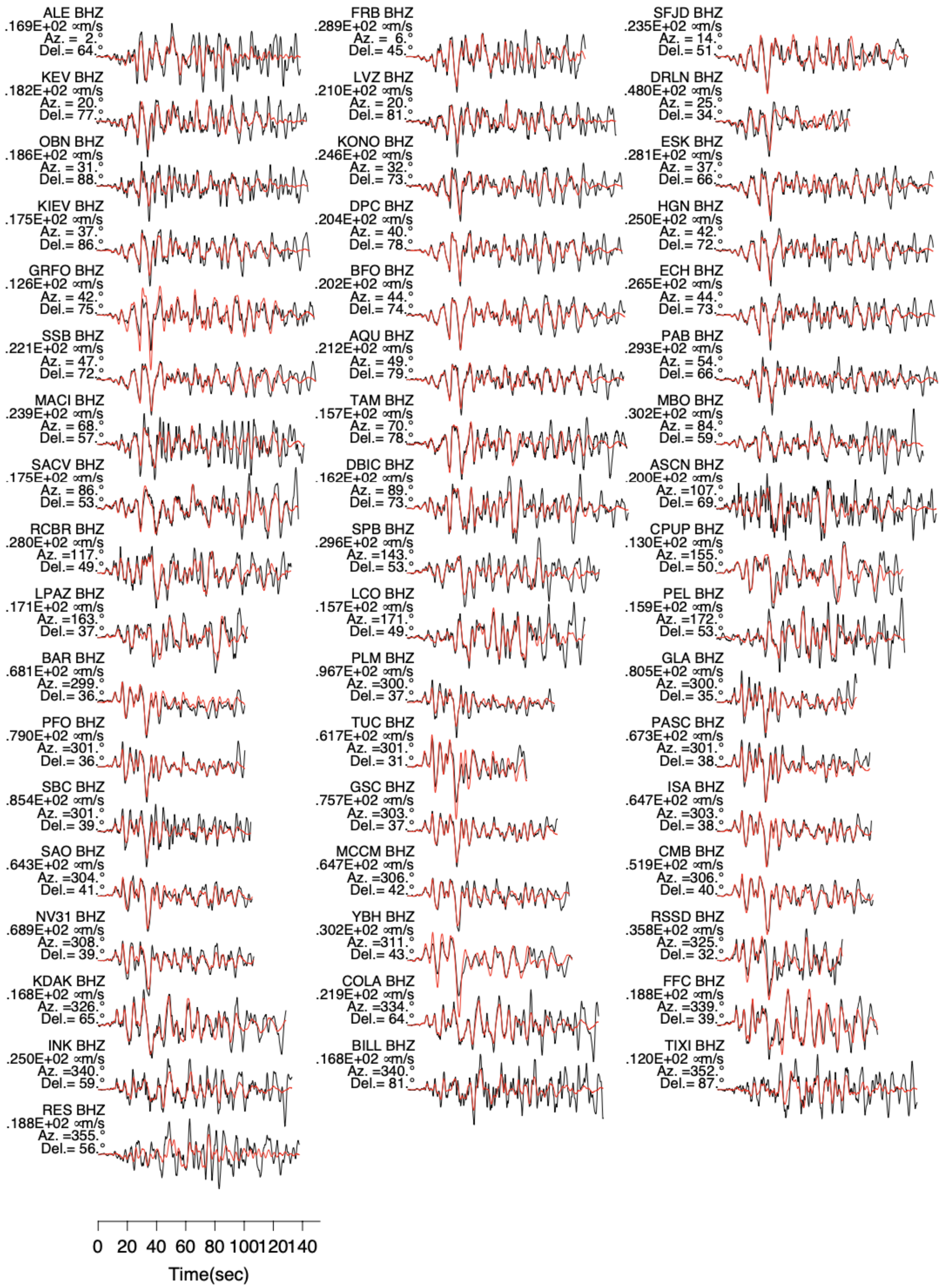

Figure S1. Waveform fitting at all stations between observed (black) and synthetic waveforms (red). Station code, azimuth, and epicentral distance are shown on top-left of the waveform.

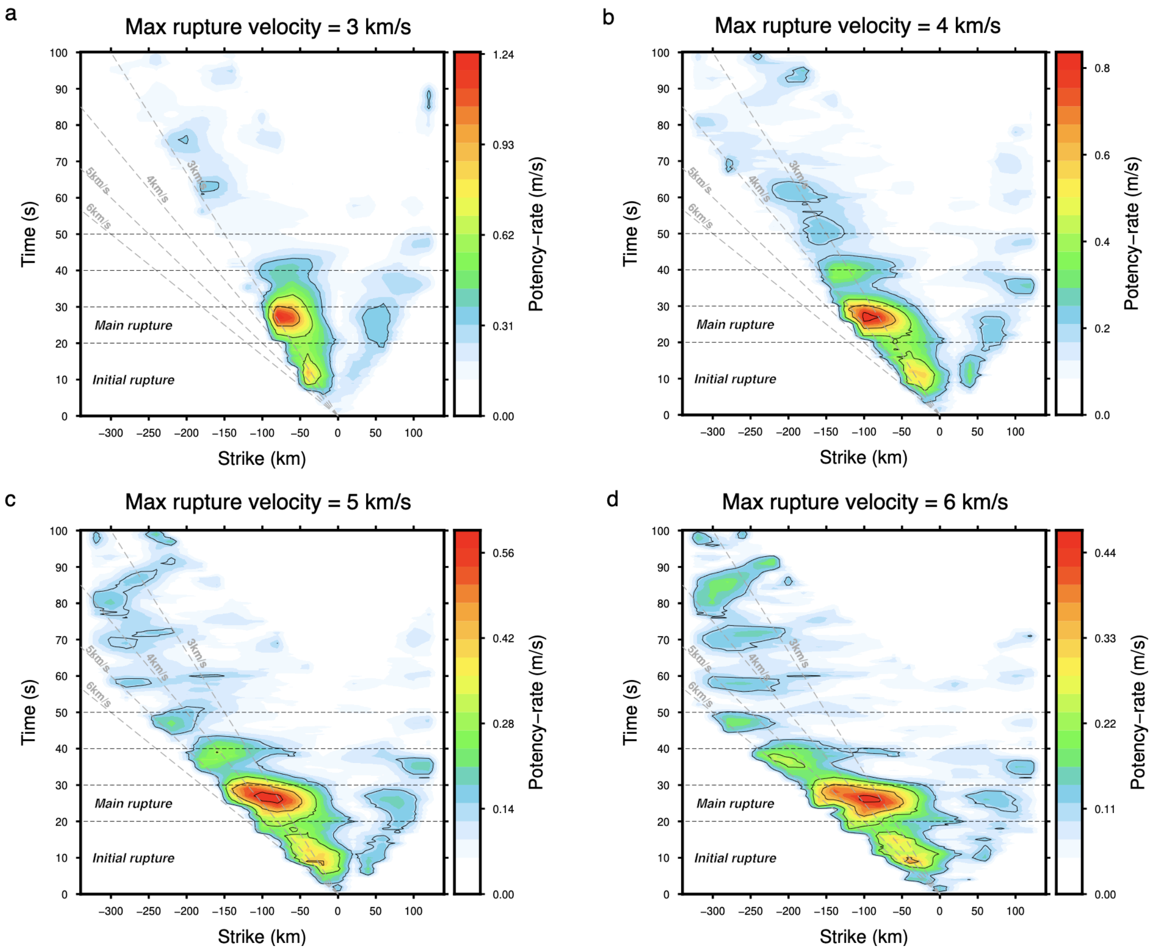

Figure S2. The comparison of spatiotemporal distribution of potency-rate density along the strike. Each panel shows the result with the assumption of maximum rupture velocity at (a) 3 km/s, (b) 4 km/s, (c) 5 km/s, and (d) 6 km/s. The gray dashed lines show the reference rupture-front speeds.

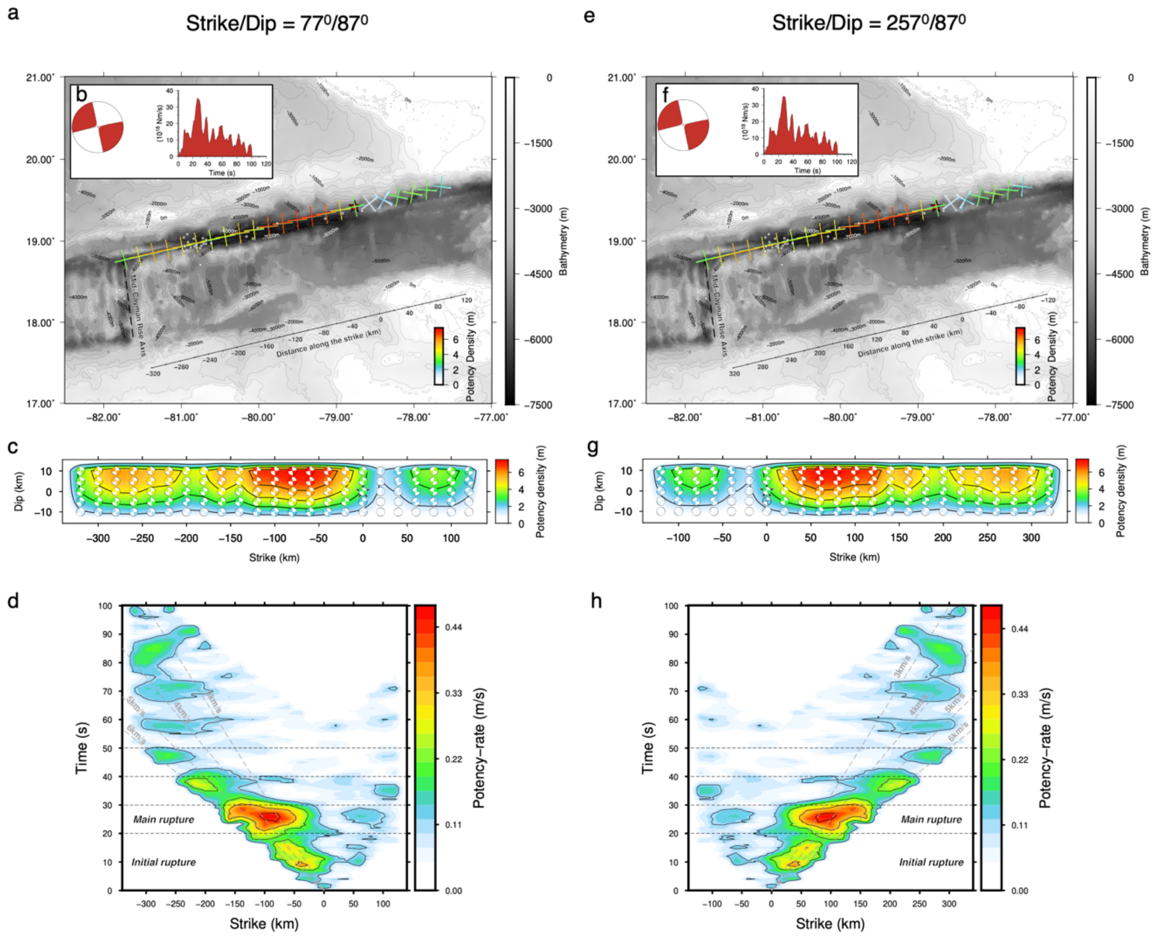

Figure S3. The results for the different model faults. (**a**) Map-view of the static potency density distribution of the model fault plane strike/dip : 77°/87°. The nodal plane (cross-mark) is extracted from the potency density tensor of each source knot by summing all the potency-density tensors along the dip direction for each strike direction. The contour line with 500 m intervals show the bathymetric feature (same as Fig. 2a). The gray circles are 1-week aftershocks, and the red star is the epicenter. (**b**) The information of moment-rate function and the total moment tensor solution of assumed model fault plane strike/dip : 77°/87°. (**c**) The cross-section (on model fault plane) of potency density and its focal mechanism of each source knot. The black star denotes the hypocenter. (**d**) The potency-rate density of rupture propagation along the strike. The gray dashed lines represent rupture speed. (**e**) to (**h**) The static distribution of potency density and its potency-rate density of rupture propagation of assumed model fault plane strike/dip : 257°/87° by the same details as (**a**) to (**d**).

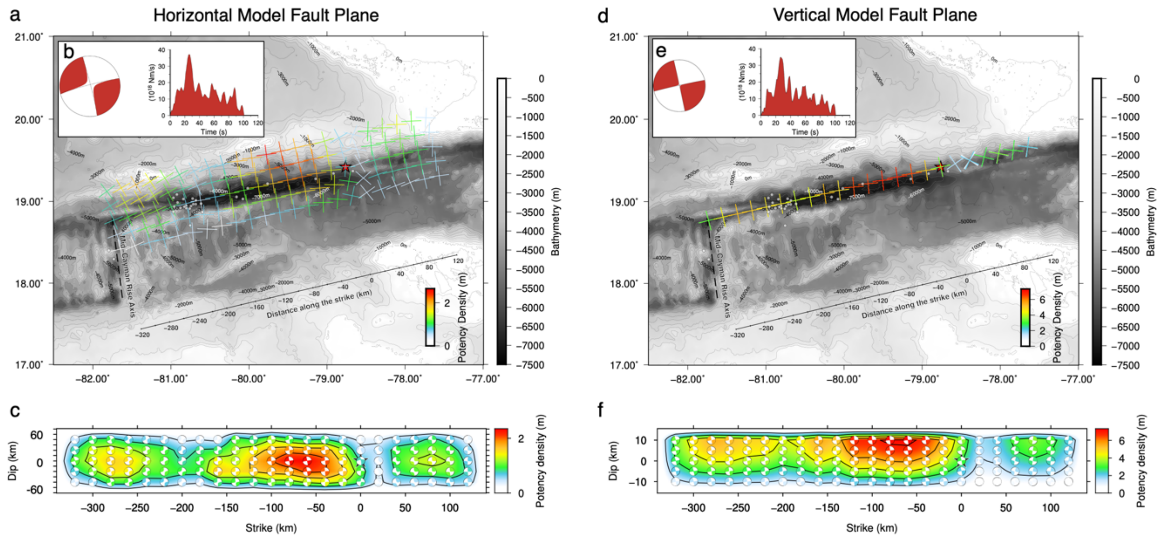

Figure S4. Comparison of the models with the horizontal and the vertical model fault planes. (a) The map view of static potency density distribution using the horizontal model fault (dip = 0°). The nodal planes (cross marker) for each location represent a potency density tensor, calculated by summing all the potency density tensors along the dip direction for each strike direction. All the potency density tensors are shown in Fig. 2d. The gray circle shows the 1-week aftershocks (USGS). The contour represents the bathymetry (GEBCO, 2020). (b) The total moment tensor solution estimated from our finite-fault model, using a lower-hemisphere stereographic projection, and the moment-rate function. (c) The cross-section of the static potency density distribution. The focal mechanism is presented by the beach ball at each source knot, plotted using a lower-hemisphere stereographic projection (not a view form side but from above). (d–f) Same as Fig. S4a–c, but for the result with using the vertical model fault (dip = 90°).

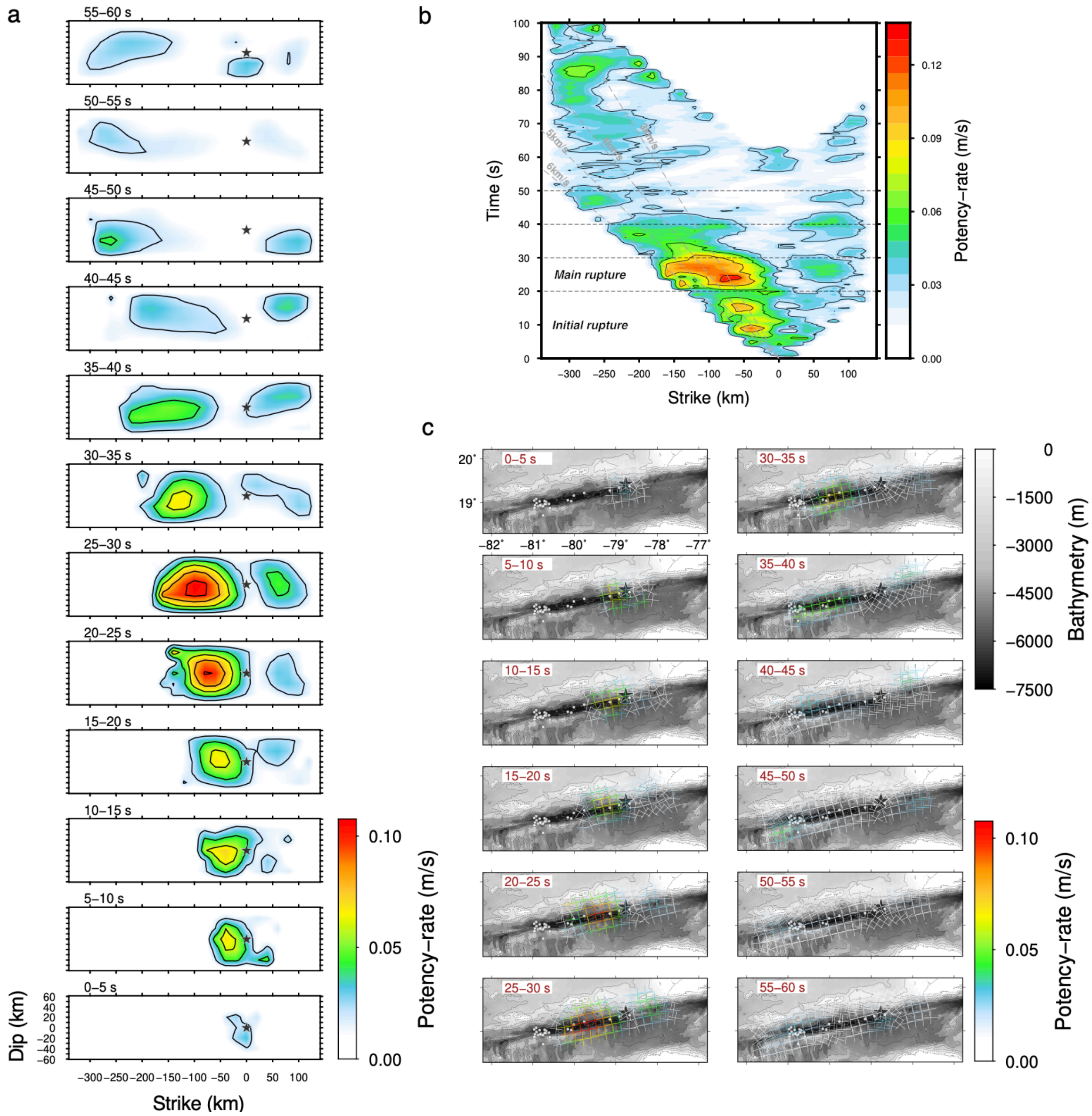

Figure S5. Spatiotemporal distribution of potency-rate density using the horizontal model plane. (a) The snapshots of the rupture propagation. The potency-rate density is averaged within each time window. The black star is the hypocenter, and the color contour shows the potency-rate density. (b) The potency-rate density distribution projected along the model strike. The gray dashed lines represent the reference rupture speeds. (c) The map-view snapshots of the averaged potency-rate density within each time window. The cross marker shows the focal mechanism extracted from the resultant potency-rate density tensor. The background contour shows the bathymetry (GEBCO, 2020). The black star and gray circle denote the epicenter and the 1-week aftershocks (USGS).

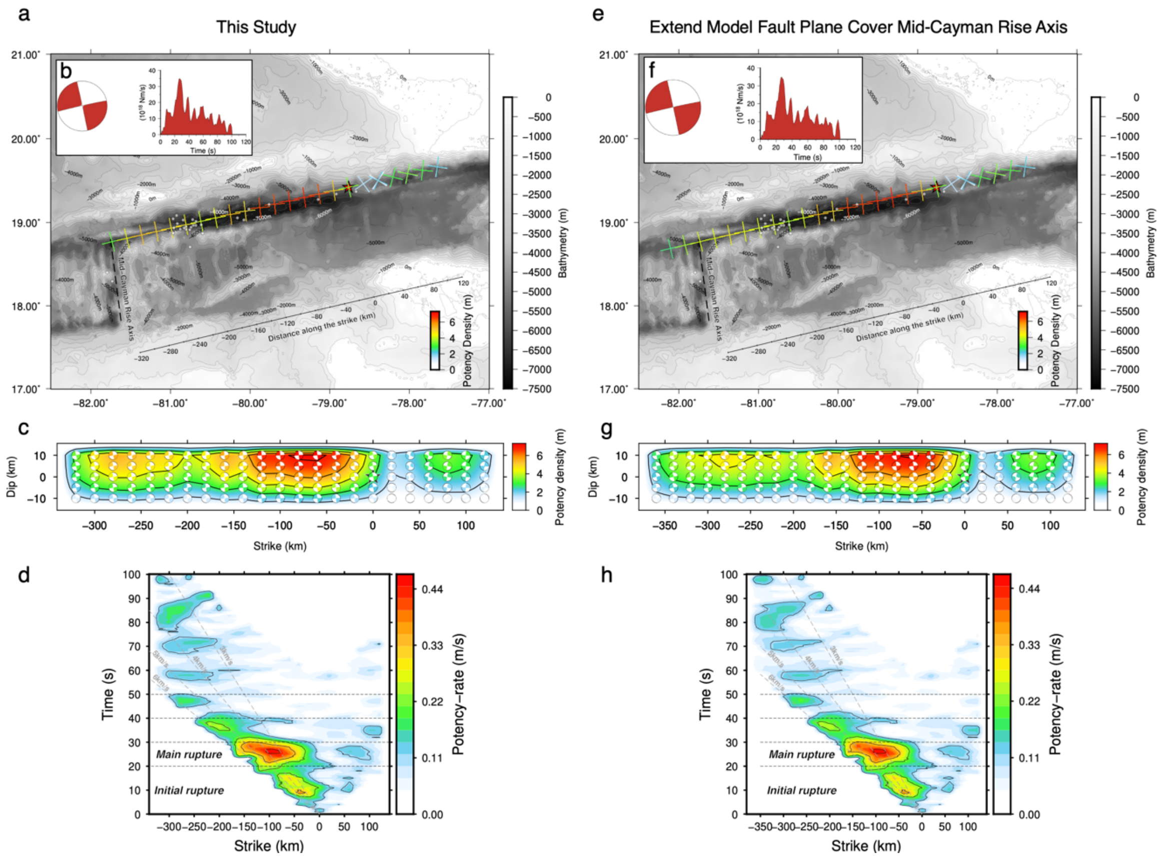

Figure S6. Comparison of the models with different model-fault lengths. (a) The map view of static potency density distribution. The nodal planes (cross marker) for each location represent a potency density tensor, calculated by summing all the potency density tensors along the dip direction for each strike direction. All the potency density tensors are shown in Fig. 2d. The gray circle shows the 1-week aftershocks (USGS). The contour represents the bathymetry (GEBCO, 2020). (b) The total moment tensor solution estimated from our finite-fault model, using a lower-hemisphere stereographic projection, and the moment-rate function. (c) The cross-section of the static potency density distribution. The focal mechanism is presented by the beach ball at each source knot, plotted using a lower-hemisphere stereographic projection (not a view form side but from above). (d) The potency-rate density distribution projected along the model strike. The gray dashed lines represent the reference rupture speeds. (e–h) Same as Fig. S6a–d, but for the result using the extended model-fault length.

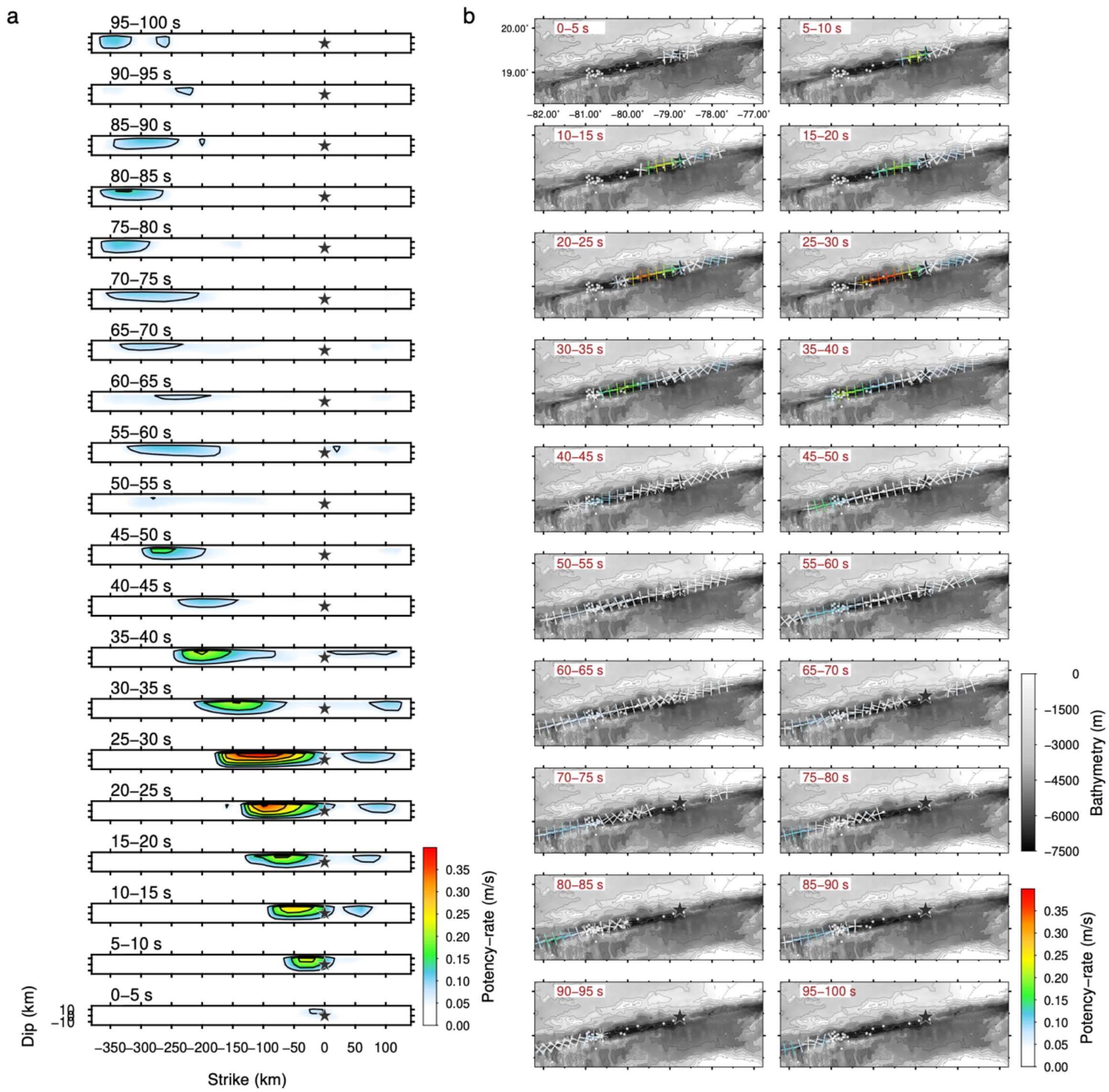

Figure S7. Spatiotemporal distribution of potency-rate density for the extended model-plane length (Fig. S7). (a) The snapshots of the rupture propagation. The potency-rate density is averaged within each time window. The black star is the hypocenter, and the color contour shows the potency-rate density. (b) The map-view snapshots of the averaged potency-rate density within each time window. The cross marker shows the focal mechanism extracted from the resultant potency-rate density tensor. The background contour shows the bathymetry (GEBCO, 2020). The black star and gray circle denote the epicenter and the 1-week aftershocks (USGS).

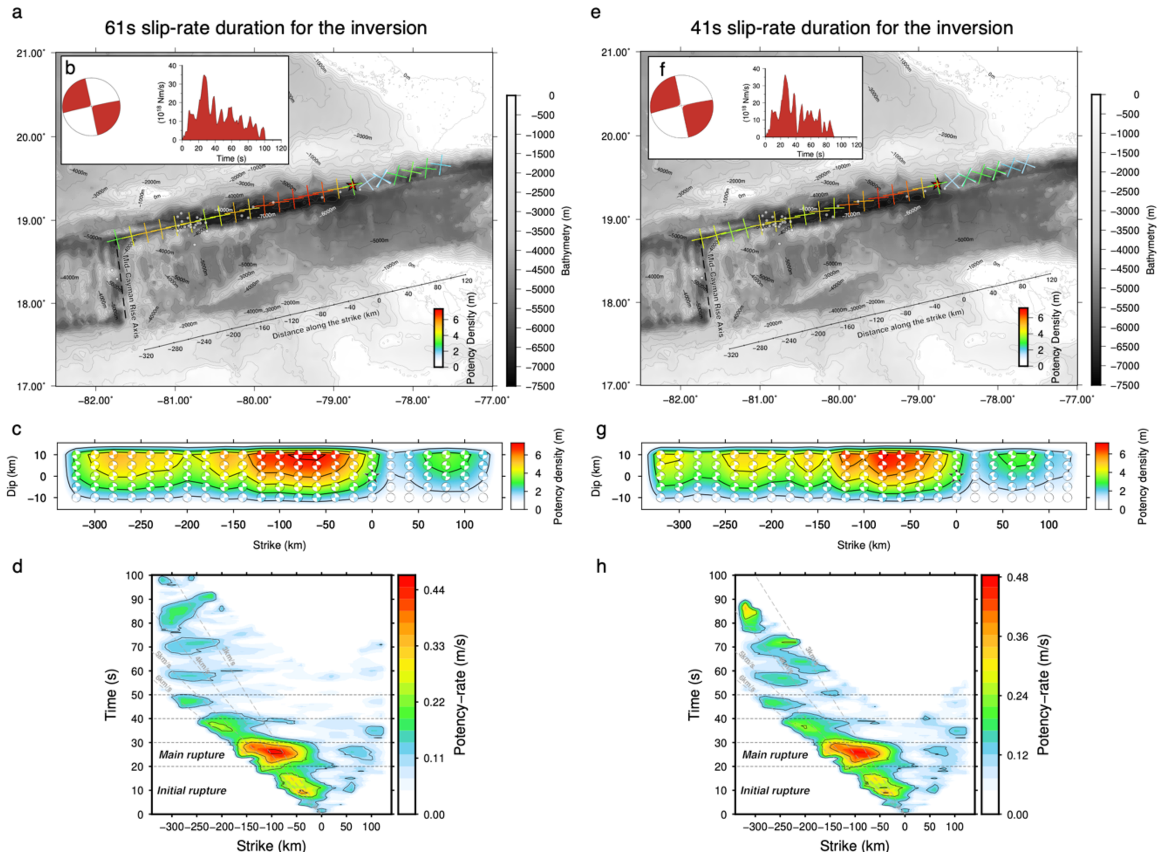

Figure S8. Comparison of the models with different assumption of duration of slip-rate function. (a) The map view of static potency density distribution by adopting the duration of slip-rate function at 61 s. The nodal planes (cross marker) for each location represent a potency density tensor, calculated by summing all the potency density tensors along the dip direction for each strike direction. All the potency density tensors are shown in Fig. 2d. The gray circle shows the 1-week aftershocks (USGS). The contour represents the bathymetry (GEBCO, 2020). (b) The total moment tensor solution estimated from our finite-fault model, using a lower-hemisphere stereographic projection, and the moment-rate function. (c) The cross-section of the static potency density distribution. The focal mechanism is presented by the beach ball at each source knot, plotted using a lower-hemisphere stereographic projection (not a view form side but from above). (d) The potency-rate density distribution projected along the model strike. The gray dashed lines represent the reference rupture speeds. (e–h) Same as Fig. S8a–d, but for the result adopting the duration of slip-rate function at 41 s.

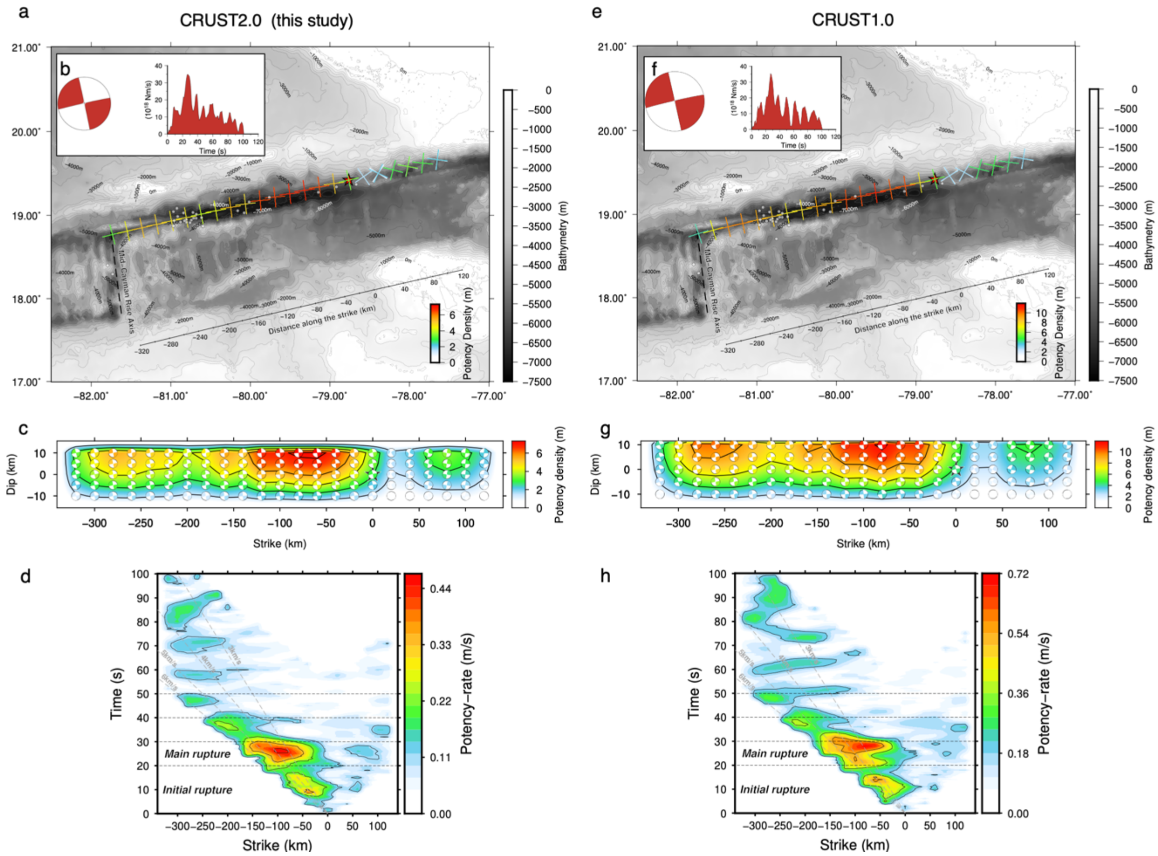

Figure S9. Comparison of the models with different near-field velocity structures. (a) The map view of static potency density distribution using the CRUST2.0 (Bassin et. al., 2000; USGS, 2020). The nodal planes (cross marker) for each location represent a potency density tensor, calculated by summing all the potency density tensors along the dip direction for each strike direction. All the potency density tensors are shown in Fig. 2d. The gray circle shows the 1-week aftershocks (USGS). The contour represents the bathymetry (GEBCO, 2020). (b) The total moment tensor solution estimated from our finite-fault model, using a lower-hemisphere stereographic projection, and the moment-rate function. (c) The cross-section of the static potency density distribution. The focal mechanism is presented by the beach ball at each source knot, plotted using a lower-hemisphere stereographic projection (not a view form side but from above). (d) The potency-rate density distribution projected along the model strike. The gray dashed lines represent the reference rupture speeds. (e–h) Same as Fig. S9a–d, but for the result using the CRUST1.0 (Laske et. al., 2013).

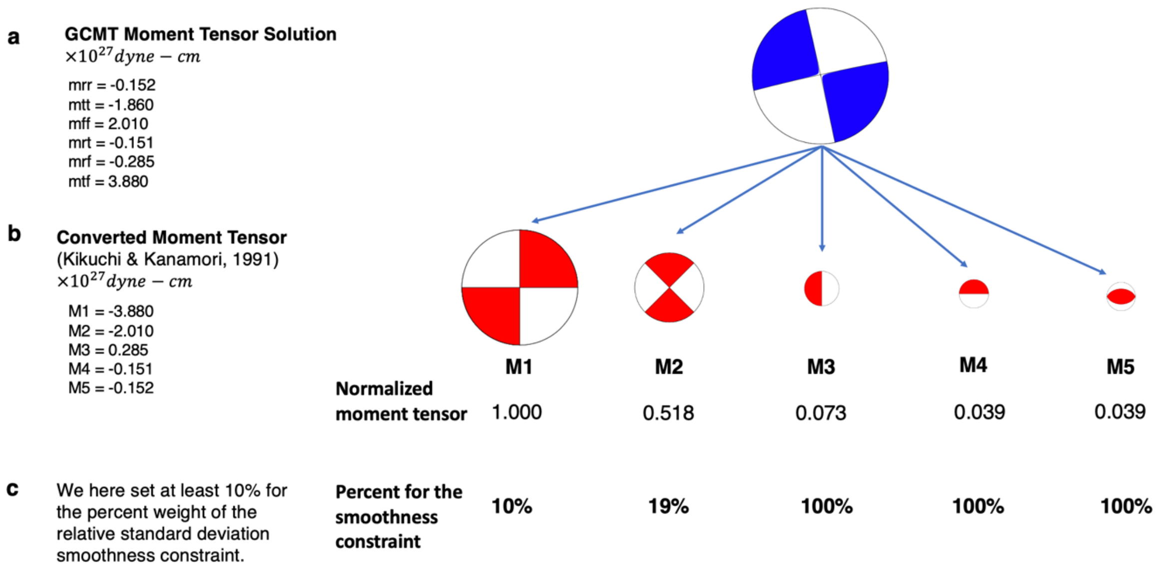

Figure S10. Summary of our new framework of inversion adopting relative weight for the smoothness constraint. The GCMT moment tensor solution of the 2020 Caribbean earthquake (GCMT, 2020) is divided into the 5 basis-moment tensors (M1 to M5, Kikuchi and Kanamori, 1991). Then, we determine the relative weight for each moment tensor component for the smoothness constraint.

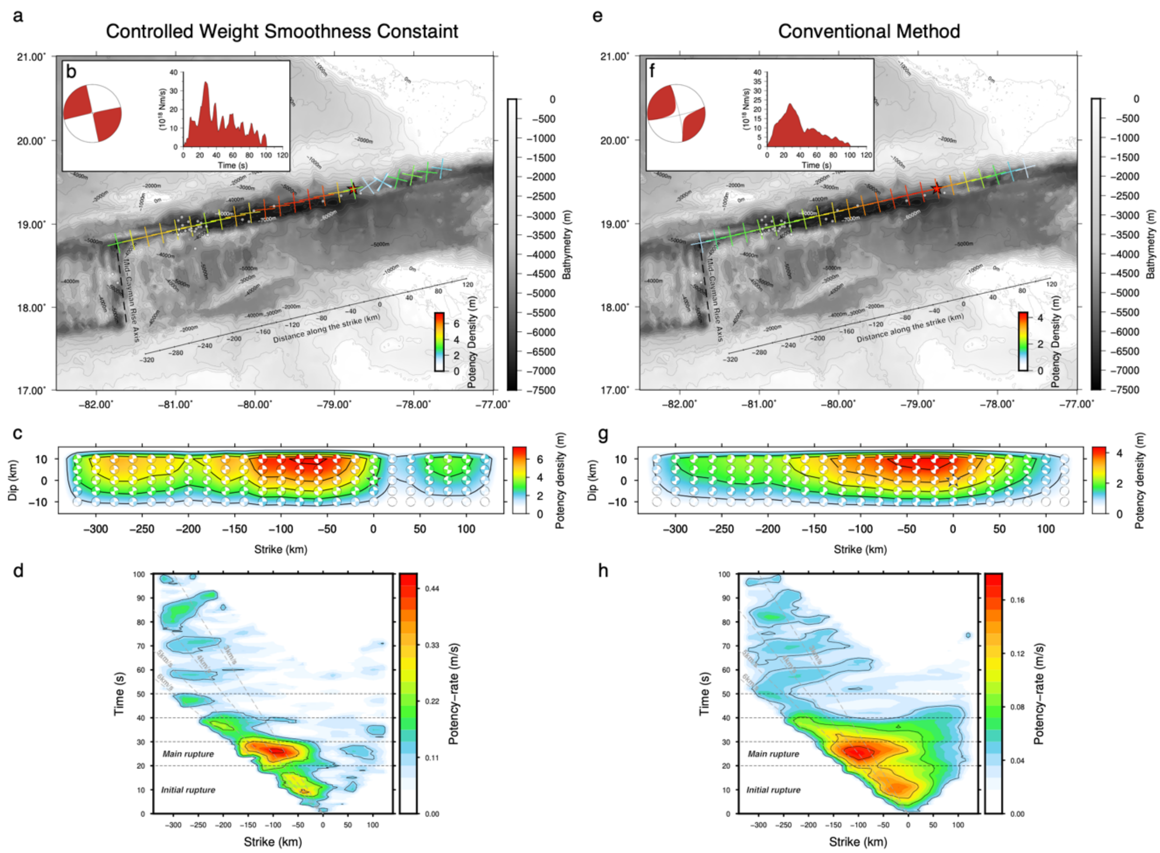

Figure S11. Comparison of the models adopting and not-adopting the relative weights for basis-moment tensors. (a) The map view of static potency density distribution by adopting the relative weights for basis-moment tensors. The nodal planes (cross marker) for each location represent a potency density tensor, calculated by summing all the potency density tensors along the dip direction for each strike direction. All the potency density tensors are shown in Fig. 2d. The gray circle shows the 1-week aftershocks (USGS). The contour represents the bathymetry (GEBCO, 2020). (b) The total moment tensor solution estimated from our finite-fault model, using a lower-hemisphere stereographic projection, and the moment-rate function. (c) The cross-section of the static potency density distribution. The focal mechanism is presented by the beach ball at each source knot, plotted using a lower-hemisphere stereographic projection (not a view form side but from above). (d) The potency-rate density distribution projected along the model strike. The gray dashed lines represent the reference rupture speeds. (e–h) Same as Fig. S11a–d, but for the result without adopting the relative weights for basis-moment tensors.

Table S1. CRUST2.0 structural velocity model being used in this study (Bassin et. al., 2000; USGS, 2020).

V_P (km/s)	V_S (km/s)	Density (10^3 kg/m^3)	Thickness (km)
1.50	0.01	1.02	4.0
2.20	1.10	2.20	1.0
5.00	2.50	2.60	2.5
6.60	3.65	2.90	4.0
7.10	3.90	3.05	5.0
8.08	4.47	3.38	0.0

Table S2. CRUST1.0 structural velocity model (Laske et. al., 2013).

V_P (km/s)	V_S (km/s)	Density (10^3 kg/m^3)	Thickness (km)
1.50	0.01	1.02	3.95
2.00	0.55	1.93	4.75
5.00	2.70	2.55	5.38
6.50	3.70	2.85	6.66
7.10	4.05	3.05	11.12
8.09	4.49	3.33	0.00

References

Bassin, C., Laske, G. and Masters, G. (2000), The Current Limits of Resolution for Surface Wave Tomography in North America, EOS Trans AGU, 81, F897.

GCMT. (2020), Mw 7.7 Cuba Region. Retrieved January 28, 2020, from https://www.globalcmt.org/cgi-bin/globalcmt-cgi-bin/CMT5/form?itype=ymd&yr=2020&mo=1&day=28&oyr=1976&omo=1&oday=1&jyr=1976&jday=1&ojyr=1976&ojday=1&otype=nd&nday=1&lmw=7&umw=10&lms=0&ums=10&lmb=0&umb=10&llat=-90&ulat=90&llon=-180&ulon=180&lhd=0&uhd=1000&l.

GEBCO Compilation Group, (2020), GEBCO 2020 Grid (Gridded Bathymetry Data Download). doi:10.5285/a29c5465-b138-234d-e053-6c86abc040b9.

Kikuchi, M., & Kanamori, H. (1991), Inversion of Complex Body Waves-III. *Bulletin of the Seismological Society of America*, *81*(6), 2335–2350. https://doi.org/10.1016/0031-9201(86)90048-8.

Laske, G., Masters., G., Ma, Z. and Pasyanos, M. (2013), Update on CRUST1.0 -A 1-degree Global Model of Earth’s Crust, Geophys. Res. Abstract, 15, Abstract EGU2013-2658.

USGS. (2020), M 7.7 - 123km NNW of Lucea, Jamaica. Retrieved January 28, 2020, from https://earthquake.usgs.gov/earthquakes/eventpage/us60007idc/executive.